



Fractional nonlocal strain-gradient isogeometric analysis of porous functionally graded piezoelectric microplates resting on elastic substrates

Sule Adekunle Jimoh ^{a,*}, Olorunsola Oriola Niyi ^b, Adebola Samuel Adeoye ^a, Daramola Oluwatosin Bunmi ^c, Ezekiel Olaoluwa Omole ^d

^aDepartment of Mathematical Sciences, Achievers University, Owo, Ondo State, Nigeria

^bDepartment of Mathematical Sciences, Federal University of Education, Kontagora, Niger State, Nigeria

^cDepartment of Geological Sciences, Faculty of Natural and Applied Sciences, Achievers University, Owo, Ondo State, Nigeria

^dDepartment of Mathematics, Federal University of Technology and Environmental Sciences, Iyin-Ekiti, Ekiti State, Nigeria

Abstract

Existing strain-gradient models for piezoelectric microplates often capture local microstructural size effects but do not simultaneously represent long-range spatial interactions, porosity-induced material degradation, electromechanical coupling, and elastic-substrate effects within a unified computational framework. This paper develops a fractional nonlocal strain-gradient isogeometric formulation for the free vibration analysis of porous functionally graded piezoelectric microplates resting on elastic substrates. The plate kinematics are described using higher-order shear deformation theory, while the fractional Laplacian operator is introduced to model spatial nonlocality and the strain-gradient term accounts for intrinsic length-scale stiffening. The governing equations are derived from Hamilton's variational principle by incorporating thickness-dependent elastic, piezoelectric, dielectric, and density properties. The Winkler–Pasternak foundation model is used to represent substrate interaction, and isogeometric analysis is adopted to satisfy the higher-order continuity requirements of the enriched formulation. The proposed model is validated against published benchmark results in the classical and strain-gradient limits, with percentage-error comparisons included. Parametric results show that porosity reduces the natural frequencies, whereas strain-gradient effects and elastic foundation stiffness increase them. The fractional order, nonlocal interaction length, applied electric voltage, and porosity pattern significantly influence the effective stiffness and vibration response. The proposed formulation provides a physically consistent framework for designing smart porous piezoelectric microplates used in microelectromechanical systems, sensors, actuators, and micro-energy harvesting systems.

DOI:10.46481/asr.2026.5.2.502

Keywords: Fractional nonlocal strain–gradient, Porous piezoelectric microplates, Isogeometric analysis, Elastic substrate interaction.

Article History:

Received: 31 March 2026

Received in revised form: 11 May 2026

Accepted for publication: 20 May 2026


Available online: 01 June 2026

© 2026 The Author(s). Published by the [Nigerian Society of Physical Sciences](#) under the terms of the [Creative Commons Attribution 4.0 International license](#). Further distribution of this work must maintain attribution to the author(s) and the published article's title, journal citation, and DOI.

1. Introduction

The rapid miniaturization of engineering systems has increased the use of microelectromechanical systems (MEMS), smart sensors, biomedical micro-devices, precision actuators, resonators, and micro-energy harvesting devices. In these applications,

*Corresponding author Tel. No.: +234-706-893-0993.

Email address: sajimoh@achievers.edu.ng (Sule Adekunle Jimoh )

piezoelectric microplates are important structural components because they combine load-bearing capacity with electromechanical coupling. This coupling enables direct conversion between mechanical deformation and electrical response, making piezoelectric microplates suitable for sensing, actuation, adaptive vibration control, and multifunctional smart structures.

When the characteristic dimensions of structural components are reduced to the micro- and nano-scale, the predictions of classical continuum mechanics become less reliable because classical local theories do not include intrinsic material length-scale effects and long-range spatial interactions. Yang *et al.* [1] introduced a couple-stress-based strain-gradient theory to incorporate size-dependent elastic effects into continuum modelling. Lam *et al.* [2] provided experimental and theoretical evidence that strain-gradient elasticity captures microstructural size effects absent in classical elasticity. These theories have improved the modelling of bending, buckling, and vibration responses of microstructured beams and plates. However, strain-gradient-type theories mainly describe local microstructural stiffening and do not fully account for long-range spatial interactions.

Nonlocal elasticity theory provides a complementary approach for modelling small-scale behaviour. Eringen [3] stated that the stress at a material point may depend not only on the local strain at that point but also on the strain field in a finite surrounding region. This idea was further developed within nonlocal continuum field theory by Eringen [4]. This makes nonlocal elasticity suitable for capturing stiffness softening and frequency shifts in microplates and nanoplates. Nevertheless, conventional nonlocal models may not include the higher-order stiffening mechanism associated with strain-gradient effects. Therefore, the use of only nonlocal elasticity or only strain-gradient elasticity may provide an incomplete description of porous smart microplates.

Porous functionally graded piezoelectric materials introduce further modelling complexity because their elastic, inertial, dielectric, and piezoelectric properties vary through the thickness. Porosity also affects stiffness, density, and electromechanical coupling. Wu and Lin [5] investigated the free vibration of porous functionally graded piezoelectric microplates resting on elastic media and subjected to electric voltage, showing that porosity, voltage, and elastic support significantly influence the vibration response. Liang *et al.* [6] demonstrated the usefulness of isogeometric analysis for functionally graded piezoelectric plate-type structures resting on Winkler elastic foundations. These studies confirm that accurate prediction of porous piezoelectric microplate behaviour requires a model that captures material gradation, porosity distribution, size dependency, electrical coupling, and substrate interaction.

Several computational and theoretical advances have supported the analysis of size-dependent plate structures. Hughes *et al.* [7] introduced isogeometric analysis as a computational method that combines exact geometric representation with smooth spline basis functions. Thai *et al.* [8] applied isogeometric analysis to size-dependent functionally graded microplates based on modified strain-gradient elasticity. Thai *et al.* [9] studied the size-dependent free vibration of multilayer functionally graded graphene-platelet-reinforced microplates. Lu *et al.* [10] developed a unified size-dependent plate model based on nonlocal strain-gradient theory including surface effects. These contributions show that nonlocality, strain-gradient elasticity, and isogeometric discretization are important tools for modelling microplate vibration. However, they do not fully combine fractional nonlocality, porosity, piezoelectric coupling, temporal memory, and Winkler–Pasternak foundation interaction in one framework.

Fractional-order modelling provides a flexible way to represent spatial nonlocality. Di Paola *et al.* [11] presented a generalized elastic foundation model based on long-range interactions using integral and fractional formulations. Rahimi *et al.* [12] used fractional strain energy in the free vibration analysis of nonlocal continuum structures. These studies show that fractional operators can describe long-range interactions in a scale-sensitive manner. When combined with strain-gradient elasticity, fractional nonlocal modelling can represent the competition between nonlocal softening and microstructural stiffening. At the nanoscale, related ASR-based computational studies have also emphasized the importance of temperature-sensitive mechanical properties in nanocrystalline materials [13]. This further supports the need for scale-aware continuum modelling of microstructured smart materials.

The supporting medium also plays an important role in the vibration response of microplates. Pasternak [14] introduced a two-parameter elastic foundation model that includes both normal foundation reaction and shear interaction. Kerr [15] discussed elastic and viscoelastic foundation models, while Kerr [16] further analysed a new foundation model for structural applications. These foundation models show that the surrounding medium can substantially alter the stiffness and vibration characteristics of plates. Hence, the Winkler–Pasternak model provides a more realistic representation of substrate interaction than the single-parameter Winkler model.

Phong and Hung [17] analysed the size-dependent free vibration of porous piezoelectric microplates resting on elastic substrates using modified strain-gradient theory, higher-order shear deformation theory, and isogeometric analysis. That study provides useful benchmark results for validating strain-gradient piezoelectric microplate models. However, the combined effects of fractional nonlocality, temporal memory, porosity, piezoelectric coupling, and Winkler–Pasternak substrate interaction remain insufficiently developed within a unified isogeometric formulation.

In view of the above literature, a clear research gap remains. Existing studies have generally treated nonlocality, strain-gradient elasticity, porosity, piezoelectric coupling, temporal memory, and elastic substrate interaction as separate or only partially coupled effects. For porous functionally graded piezoelectric microplates operating in realistic micro-scale environments, these mechanisms act simultaneously and should therefore be represented within a unified theoretical and computational framework.

The present study addresses this gap by developing a fractional nonlocal strain-gradient isogeometric formulation for the free vibration analysis of porous functionally graded piezoelectric microplates resting on elastic substrates. The model combines fractional Laplacian-based nonlocality, strain-gradient elasticity, higher-order shear deformation theory, piezoelectric coupling, temporal fractional memory, and Winkler–Pasternak foundation interaction within a unified framework.

The specific objectives of this study are: (i) to formulate the governing equations using Hamilton’s variational principle; (ii) to incorporate fractional nonlocality, strain-gradient elasticity, electromechanical coupling, temporal memory, and elastic foundation effects; (iii) to discretize the weak form using isogeometric analysis; (iv) to validate the formulation using benchmark solutions and percentage-error comparison; and (v) to investigate the effects of porosity coefficient, porosity pattern, fractional order, non-local length scale, strain-gradient parameter, applied electric voltage, foundation stiffness, and boundary conditions on the natural frequencies.

2. Materials and methods

2.1. Material characteristics of the fractional nonlocal porous functionally graded piezoelectric microplate

A porous functionally graded piezoelectric (FGPP) microplate of thickness h resting on an elastic substrate is considered, as illustrated in Figure 1. The in-plane dimensions of the microplate are denoted by a and b , while the thickness coordinate is $z \in [-h/2, h/2]$. The effective material properties are assumed to vary continuously through the thickness due to the combined effects of functional gradation and porosity distribution.

In the present formulation, the thickness-dependent elastic stiffness coefficients, mass density, piezoelectric constants, and dielectric coefficients are denoted by $\mathbb{C}_{ijkl}(z)$, $\rho(z)$, $\mathbb{P}_{kij}(z)$, and $\mathbb{K}_{ij}(z)$, respectively. Three representative porosity distribution patterns, denoted by D-I, D-II, and D-III, are adopted to describe the degradation of the effective electromechanical properties through the thickness.

Porosity distribution models. For the three porosity distributions considered in this study, namely D-I (symmetric mid-plane porosity distribution), D-II (symmetric surface-biased porosity distribution), and D-III (uniform porosity distribution), the effective material properties are expressed as follows:

$$\text{D-I: Symmetric mid-plane porosity} \quad \left\{ \begin{array}{l} \mathbb{C}_{ijkl}(z) = \mathbb{C}_{ijkl}^{(1)} \left(1 - \eta \cos \frac{\pi z}{h} \right), \\ \rho(z) = \rho^{(1)} \left(1 - \eta_\rho \cos \frac{\pi z}{h} \right), \\ \mathbb{P}_{kij}(z) = \mathbb{P}_{kij}^{(1)} \left(1 - \eta \cos \frac{\pi z}{h} \right), \\ \mathbb{K}_{ij}(z) = \mathbb{K}_{ij}^{(1)} \left(1 - \eta \cos \frac{\pi z}{h} \right). \end{array} \right. \quad (1)$$

$$\text{D-II: Symmetric surface-biased porosity} \quad \left\{ \begin{array}{l} \mathbb{C}_{ijkl}(z) = \mathbb{C}_{ijkl}^{(1)} \left[1 - \eta^* \left(1 - \cos \frac{\pi z}{h} \right) \right], \\ \rho(z) = \rho^{(1)} \left[1 - \eta_\rho^* \left(1 - \cos \frac{\pi z}{h} \right) \right], \\ \mathbb{P}_{kij}(z) = \mathbb{P}_{kij}^{(1)} \left[1 - \eta^* \left(1 - \cos \frac{\pi z}{h} \right) \right], \\ \mathbb{K}_{ij}(z) = \mathbb{K}_{ij}^{(1)} \left[1 - \eta^* \left(1 - \cos \frac{\pi z}{h} \right) \right]. \end{array} \right. \quad (2)$$

$$\text{D-III: Uniform porosity} \quad \left\{ \begin{array}{l} \mathbb{C}_{ijkl}(z) = \mathbb{C}_{ijkl}^{(1)} \gamma, \\ \rho(z) = \rho^{(1)} \gamma_\rho, \\ \mathbb{P}_{kij}(z) = \mathbb{P}_{kij}^{(1)} \gamma, \\ \mathbb{K}_{ij}(z) = \mathbb{K}_{ij}^{(1)} \gamma. \end{array} \right. \quad (3)$$

In equations (1)–(3), $\mathbb{C}_{ijkl}^{(1)}$, $\rho^{(1)}$, $\mathbb{P}_{kij}^{(1)}$, and $\mathbb{K}_{ij}^{(1)}$ denote the fully dense elastic, density, piezoelectric, and dielectric coefficients, respectively. The quantities η , η^* , and γ are the porosity coefficients associated with D-I, D-II, and D-III, respectively, while η_ρ , η_ρ^* , and γ_ρ are the corresponding mass-porosity coefficients.

Porosity parameter: The porosity coefficient η is evaluated from the stiffness contrast as

$$\eta = 1 - \frac{E_2}{E_1} = 1 - \frac{G_2}{G_1}, \quad 0 < \eta < 1, \quad (4)$$

where E_1 and G_1 are the maximum Young’s modulus and shear modulus, respectively, while E_2 and G_2 are the corresponding minimum values.

Table 1: Porosity coefficients assigned to the different porosity distribution patterns.

η	η^*	γ
0.05	0.0876	0.9682
0.15	0.2628	0.9045
0.25	0.4380	0.8408
0.35	0.6132	0.7772
0.45	0.7884	0.7135
0.55	0.9636	0.6499

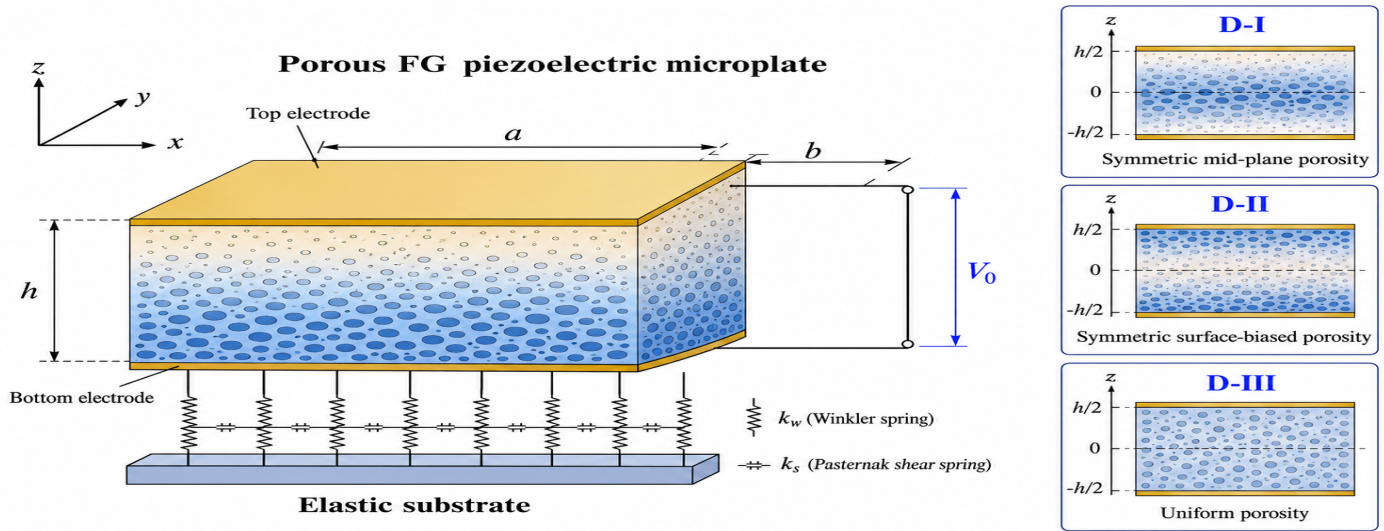


Figure 1: Schematic of the porous functionally graded piezoelectric microplate with different porosity distribution patterns.

Density–elastic modulus relation. To account for the coupling between density reduction and stiffness degradation, the density is related to the effective Young’s modulus by

$$\rho(z) = \rho^{(1)} \sqrt{\frac{E(z)}{E_1}}. \tag{5}$$

Substituting equation (5) into equations (1)–(3) gives

$$\begin{cases} 1 - \eta_\rho \cos \frac{\pi z}{h} = \sqrt{1 - \eta \cos \frac{\pi z}{h}}, \\ 1 - \eta_\rho^* \left(1 - \cos \frac{\pi z}{h}\right) = \sqrt{1 - \eta^* \left(1 - \cos \frac{\pi z}{h}\right)}, \\ \gamma_\rho = \sqrt{\gamma}. \end{cases} \tag{6}$$

Mass equivalence condition. To preserve the total mass among the different porosity patterns, the following mass-equivalence constraints are imposed:

$$\int_{-h/2}^{h/2} \sqrt{1 - \eta^* \left(1 - \cos \frac{\pi z}{h}\right)} dz = \int_{-h/2}^{h/2} \sqrt{1 - \eta \cos \frac{\pi z}{h}} dz, \quad \int_{-h/2}^{h/2} \sqrt{\gamma} dz = \int_{-h/2}^{h/2} \sqrt{1 - \eta \cos \frac{\pi z}{h}} dz. \tag{7}$$

The corresponding values of η^* and γ for selected values of η are listed in Table 1.

Table 1 shows the equivalent porosity parameters used to maintain comparable mass among the D-I, D-II, and D-III porosity patterns. As η increases, η^* increases while γ decreases, reflecting the stronger reduction of effective material properties with increasing porosity.

Figure 1 presents the geometry of the porous functionally graded piezoelectric microplate with in-plane dimensions a and b , thickness h , and applied electric voltage V_0 . The D-I, D-II, and D-III subfigures represent the porosity distributions used in equations (1)–(3).

2.2. Governing equations

The governing equations are formulated using a refined higher-order shear deformation theory (HSDT). Let (x, y) denote the in-plane coordinates and $z \in [-h/2, h/2]$ denote the thickness coordinate.

2.2.1. Kinematics and displacement field

The three-dimensional displacement vector is assumed as

$$\mathbf{U}(x, y, z) = \mathbf{U}^{(0)}(x, y) + z \mathbf{U}^{(1)}(x, y) + \psi(z) \mathbf{U}^{(2)}(x, y), \tag{8}$$

where

$$\mathbf{U} = \begin{Bmatrix} U_x \\ U_y \\ U_z \end{Bmatrix}, \quad \mathbf{U}^{(0)} = \begin{Bmatrix} u \\ v \\ w \end{Bmatrix}, \quad \mathbf{U}^{(1)} = \begin{Bmatrix} -w_{,x} \\ -w_{,y} \\ 0 \end{Bmatrix}, \quad \mathbf{U}^{(2)} = \begin{Bmatrix} \theta_x \\ \theta_y \\ 0 \end{Bmatrix}. \tag{9}$$

Here, $u, v,$ and w are the mid-plane displacements, while θ_x and θ_y denote higher-order shear rotations. The thickness function is chosen as

$$\psi(z) = z - \frac{5z^3}{4h^2}, \tag{10}$$

which satisfies the traction-free transverse shear condition at the top and bottom surfaces.

2.2.2. Strain field

The strain vector is decomposed into in-plane and transverse shear components as

$$\boldsymbol{\varepsilon} = \begin{Bmatrix} \boldsymbol{\varepsilon}_m \\ \boldsymbol{\gamma}_t \end{Bmatrix} = \begin{Bmatrix} \boldsymbol{\varepsilon}^{(0)} + z \boldsymbol{\kappa} + \psi(z) \boldsymbol{\varepsilon}^{(h)} \\ \psi'(z) \boldsymbol{\gamma}^{(h)} \end{Bmatrix}, \tag{11}$$

where

$$\boldsymbol{\varepsilon}_m = \begin{Bmatrix} \varepsilon_{xx} \\ \varepsilon_{yy} \\ \gamma_{xy} \end{Bmatrix}, \quad \boldsymbol{\gamma}_t = \begin{Bmatrix} \gamma_{xz} \\ \gamma_{yz} \end{Bmatrix}. \tag{12}$$

The mid-plane strain, bending curvature, higher-order strain, and shear strain vectors are defined by

$$\boldsymbol{\varepsilon}^{(0)} = \begin{Bmatrix} u_{,x} \\ v_{,y} \\ u_{,y} + v_{,x} \end{Bmatrix}, \quad \boldsymbol{\kappa} = - \begin{Bmatrix} w_{,xx} \\ w_{,yy} \\ 2w_{,xy} \end{Bmatrix}, \quad \boldsymbol{\varepsilon}^{(h)} = \begin{Bmatrix} \theta_{x,x} \\ \theta_{y,y} \\ \theta_{x,y} + \theta_{y,x} \end{Bmatrix}, \quad \boldsymbol{\gamma}^{(h)} = \begin{Bmatrix} \theta_x \\ \theta_y \end{Bmatrix}. \tag{13}$$

2.2.3. Electric potential and electric field

The electric potential is assumed to have a mixed cosine–linear distribution through the thickness:

$$\Phi(x, y, z) = \Lambda(z) \varphi(x, y) + \frac{2z}{h} V_0, \tag{14}$$

where $\varphi(x, y)$ is the mid-plane electric potential and V_0 is the externally applied voltage. The thickness function for the electric potential is given by

$$\Lambda(z) = -\cos\left(\frac{\pi z}{h}\right). \tag{15}$$

Using $\mathbf{E} = -\nabla\Phi$, the electric field vector becomes

$$\mathbf{E} = - \begin{Bmatrix} \Lambda(z)\varphi_{,x} \\ \Lambda(z)\varphi_{,y} \\ \Lambda'(z)\varphi + \frac{2V_0}{h} \end{Bmatrix}. \tag{16}$$

2.2.4. Electromechanical constitutive relations

The porous FG piezoelectric material is governed by the three-dimensional linear piezoelectric constitutive equations

$$\sigma_{ij}(z) = \mathbb{C}_{ijkl}(z) \varepsilon_{kl} - \mathbb{P}_{kij}(z) E_k, \tag{17}$$

and

$$D_i(z) = \mathbb{P}_{ikl}(z) \varepsilon_{kl} + \mathbb{K}_{ik}(z) E_k. \tag{18}$$

The material coefficients appearing in equation (17) and equation (18) vary through the thickness according to equations (1)–(3).

2.2.5. Plane-stress reduction

For thin microplates, the transverse normal stress is assumed negligible, so that $\sigma_{zz} = 0$. After applying this plane-stress condition, the reduced electromechanical constitutive equations are written as

$$\begin{Bmatrix} \sigma_m \\ \sigma_t \end{Bmatrix} = \mathbf{C}_r(z) \begin{Bmatrix} \boldsymbol{\varepsilon}_m \\ \boldsymbol{\gamma}_t \end{Bmatrix} - \mathbf{e}_r(z) \begin{Bmatrix} \mathbf{E}_n \\ \mathbf{E}_s \end{Bmatrix}, \quad \begin{Bmatrix} D_z \\ \mathbf{D}_s \end{Bmatrix} = \mathbf{e}_r^T(z) \begin{Bmatrix} \boldsymbol{\varepsilon}_m \\ \boldsymbol{\gamma}_t \end{Bmatrix} + \mathbf{k}_r(z) \begin{Bmatrix} \mathbf{E}_n \\ \mathbf{E}_s \end{Bmatrix}. \quad (19)$$

The reduced elastic stiffness matrix is expressed as

$$\mathbf{C}_r(z) = \begin{bmatrix} \mathbf{C}_m(z) & \mathbf{0} \\ \mathbf{0} & \mathbf{C}_t(z) \end{bmatrix}, \quad (20)$$

where

$$\mathbf{C}_m(z) = \begin{bmatrix} \bar{C}_{11}(z) & \bar{C}_{12}(z) & 0 \\ \bar{C}_{12}(z) & \bar{C}_{22}(z) & 0 \\ 0 & 0 & \bar{C}_{66}(z) \end{bmatrix}, \quad \mathbf{C}_t(z) = \begin{bmatrix} \bar{C}_{55}(z) & 0 \\ 0 & \bar{C}_{44}(z) \end{bmatrix}. \quad (21)$$

The reduced piezoelectric coupling matrix is

$$\mathbf{e}_r(z) = \begin{bmatrix} \mathbf{e}_m(z) & \mathbf{0} \\ \mathbf{0} & \mathbf{e}_t(z) \end{bmatrix}, \quad (22)$$

with

$$\mathbf{e}_m(z) = \begin{bmatrix} 0 & 0 & \bar{P}_{31}(z) \\ 0 & 0 & \bar{P}_{32}(z) \\ 0 & 0 & 0 \end{bmatrix}, \quad \mathbf{e}_t(z) = \begin{bmatrix} \bar{P}_{15}(z) & 0 \\ 0 & \bar{P}_{24}(z) \end{bmatrix}. \quad (23)$$

The reduced dielectric matrix is

$$\mathbf{k}_r(z) = \begin{bmatrix} \mathbf{k}_n(z) & \mathbf{0} \\ \mathbf{0} & \mathbf{k}_s(z) \end{bmatrix}, \quad (24)$$

where

$$\mathbf{k}_n(z) = \begin{bmatrix} 0 & 0 & 0 \\ 0 & 0 & 0 \\ 0 & 0 & \bar{K}_{33}(z) \end{bmatrix}, \quad \mathbf{k}_s(z) = \begin{bmatrix} \bar{K}_{11}(z) & 0 \\ 0 & \bar{K}_{22}(z) \end{bmatrix}. \quad (25)$$

Representative reduced coefficients are obtained from the three-dimensional coefficients as

$$\bar{C}_{11}(z) = C_{11}(z) - \frac{C_{13}^2(z)}{C_{33}(z)}, \quad \bar{P}_{31}(z) = P_{31}(z) - \frac{P_{33}(z)C_{13}(z)}{C_{33}(z)}, \quad \bar{K}_{33}(z) = K_{33}(z) + \frac{P_{33}^2(z)}{C_{33}(z)}. \quad (26)$$

The coefficients in equation (26) remain functions of z because the original material coefficients vary through the thickness.

2.3. Fractional nonlocal strain–gradient constitutive model

To account for both long-range interactions and microstructural size effects, a fractional nonlocal strain–gradient constitutive model is adopted.

2.3.1. Fractional nonlocal operator

The fractional nonlocal operator is defined using the Riesz fractional Laplacian:

$$(-\Delta)^{\alpha/2} \boldsymbol{\varepsilon}(\mathbf{x}) = C_{n,\alpha} \int_{\mathbb{R}^n} \frac{\boldsymbol{\varepsilon}(\mathbf{x}) - \boldsymbol{\varepsilon}(\mathbf{y})}{|\mathbf{x} - \mathbf{y}|^{n+\alpha}} d\mathbf{y}, \quad 0 < \alpha \leq 2, \quad (27)$$

where $C_{n,\alpha}$ is a normalization constant and α controls the degree of spatial nonlocality.

2.3.2. Enriched strain measure

The effective fractional nonlocal strain is introduced as

$$\hat{\boldsymbol{\varepsilon}} = \boldsymbol{\varepsilon} - \ell_f^\alpha (-\Delta)^{\alpha/2} \boldsymbol{\varepsilon}, \quad (28)$$

where ℓ_f is the fractional nonlocal length scale.

The strain-gradient contribution is represented through the higher-order energy density

$$W_{sg} = \frac{1}{2} \left[\ell_1^2 \nabla \boldsymbol{\varepsilon} : \nabla \boldsymbol{\varepsilon} + \ell_2^2 \nabla (\nabla \cdot \mathbf{u}) \cdot \nabla (\nabla \cdot \mathbf{u}) + \ell_3^2 \nabla^2 \mathbf{u} : \nabla^2 \mathbf{u} \right], \tag{29}$$

where ℓ_1 , ℓ_2 , and ℓ_3 are intrinsic material length-scale parameters.

The stress–strain relation incorporating fractional nonlocality and strain-gradient effects is written as

$$\boldsymbol{\sigma} = \mathbf{C}(z) \hat{\boldsymbol{\varepsilon}} + \mathbf{C}(z) \ell_g^2 \nabla^2 \boldsymbol{\varepsilon} - \mathbf{e}^T(z) \mathbf{E}, \tag{30}$$

and the electric displacement vector is

$$\mathbf{D} = \mathbf{e}(z) \hat{\boldsymbol{\varepsilon}} + \mathbf{k}(z) \mathbf{E}. \tag{31}$$

The tensors $\mathbf{C}(z)$, $\mathbf{e}(z)$, and $\mathbf{k}(z)$ in equation (30) and equation (31) are obtained from the thickness-dependent material properties defined in equations (1)–(3).

Substituting equation (30) into the virtual strain energy gives

$$\delta U = \int_{\Omega} \left[\delta \boldsymbol{\varepsilon}^T \mathbf{C}(z) \hat{\boldsymbol{\varepsilon}} + \ell_g^2 \nabla \delta \boldsymbol{\varepsilon}^T \mathbf{C}(z) \nabla \boldsymbol{\varepsilon} \right] d\Omega - \int_{\Omega} \delta \boldsymbol{\varepsilon}^T \mathbf{e}^T(z) \mathbf{E} d\Omega. \tag{32}$$

2.4. Temporal fractional viscoelastic memory extension

The temporal hereditary effect is incorporated through a fractional Kelvin–Voigt-type viscoelastic contribution. The Caputo fractional derivative of order $\beta \in (0, 1]$ is defined by

$${}^C D_t^\beta f(t) = \frac{1}{\Gamma(1-\beta)} \int_0^t \frac{\dot{f}(\tau)}{(t-\tau)^\beta} d\tau, \quad 0 < \beta \leq 1, \tag{33}$$

where $\Gamma(\cdot)$ is the Gamma function.

Let the generalized strain and electric field vectors be defined as

$$\boldsymbol{\varepsilon}_g = \left\{ \begin{matrix} \boldsymbol{\varepsilon}_m \\ \boldsymbol{\gamma}_t \end{matrix} \right\}, \quad \mathbf{E}_g = \left\{ \begin{matrix} \mathbf{E}_n \\ \mathbf{E}_s \end{matrix} \right\}. \tag{34}$$

The memory-enhanced constitutive equation is expressed as

$$\boldsymbol{\sigma}_g = \mathbf{C}_r(z) \hat{\boldsymbol{\varepsilon}}_g + \mathbf{C}_v(z) {}^C D_t^\beta (\hat{\boldsymbol{\varepsilon}}_g) - \mathbf{e}_r(z) \mathbf{E}_g, \quad \mathbf{D}_g = \mathbf{e}_r^T(z) \hat{\boldsymbol{\varepsilon}}_g + \mathbf{k}_r(z) \mathbf{E}_g. \tag{35}$$

The viscoelastic tensor is taken in proportional form as

$$\mathbf{C}_v(z) = \eta_v \mathbf{C}_r(z), \quad \eta_v > 0, \tag{36}$$

where η_v is the viscoelastic intensity parameter.

The spatially enriched generalized strain used in equation (35) is

$$\hat{\boldsymbol{\varepsilon}}_g = \boldsymbol{\varepsilon}_g - \ell_f^\alpha (-\nabla^2)^{\alpha/2} \boldsymbol{\varepsilon}_g + \ell_g^2 \nabla^2 \boldsymbol{\varepsilon}_g. \tag{37}$$

With the temporal memory contribution, the internal virtual work becomes

$$\delta U = \int_{\Omega} \left[\delta \boldsymbol{\varepsilon}_g^T \mathbf{C}_r(z) \hat{\boldsymbol{\varepsilon}}_g + \delta \boldsymbol{\varepsilon}_g^T \mathbf{C}_v(z) {}^C D_t^\beta (\hat{\boldsymbol{\varepsilon}}_g) \right] d\Omega - \int_{\Omega} \delta \boldsymbol{\varepsilon}_g^T \mathbf{e}_r(z) \mathbf{E}_g d\Omega. \tag{38}$$

2.5. Variational formulation and foundation interaction

The governing equations are derived from Hamilton’s principle:

$$\delta \int_{t_1}^{t_2} (U - K + W_e + W_f) dt = 0, \tag{39}$$

where U is the strain energy, K is the kinetic energy, W_e is the electric potential energy, and W_f is the foundation potential energy. For harmonic free vibration, equation (39) gives the incremental condition

$$\delta \Pi = \delta U - \delta K + \delta W_e + \delta W_f = 0. \tag{40}$$

The strain energy is defined as

$$U = \frac{1}{2} \int_{\Omega} \int_{-h/2}^{h/2} (\boldsymbol{\varepsilon}^T \boldsymbol{\sigma} - \mathbf{E}^T \mathbf{D}) dz d\Omega. \tag{41}$$

The kinetic energy is

$$K = \frac{1}{2} \int_{\Omega} \int_{-h/2}^{h/2} \rho(z) \dot{\mathbf{U}}^T \dot{\mathbf{U}} dz d\Omega. \tag{42}$$

Its variation is written as

$$\delta K = - \int_{\Omega} \delta \mathbf{d}^T \mathbf{M} \ddot{\mathbf{d}} d\Omega, \tag{43}$$

where $\mathbf{d} = \{u, v, w, \theta_x, \theta_y\}^T$ is the generalized displacement vector and \mathbf{M} is the mass matrix.

For a Winkler–Pasternak elastic substrate, the foundation energy is expressed as

$$W_f = \frac{1}{2} \int_{\Omega} (k_w w^2 + k_s |\nabla w|^2) d\Omega. \tag{44}$$

The variation of equation (44) gives

$$\delta W_f = \int_{\Omega} (k_w w - k_s \nabla^2 w) \delta w d\Omega, \tag{45}$$

where k_w and k_s denote the Winkler normal stiffness and Pasternak shear interaction coefficients, respectively.

2.6. Isogeometric discretization

The spatial discretization is performed using non-uniform rational B-spline (NURBS) basis functions. The isogeometric framework is adopted because it provides exact geometric representation and the higher-order continuity required by the strain-gradient and fractional operators.

Let $\{R_A(x, y)\}_{A=1}^{n_{cp}}$ denote the NURBS basis functions associated with n_{cp} control points. The mechanical displacement vector and electric potential are approximated as

$$\mathbf{u}^h(x, y) = \sum_{A=1}^{n_{cp}} R_A(x, y) \mathbf{q}_A, \quad \varphi^h(x, y) = \sum_{A=1}^{n_{cp}} R_A(x, y) \psi_A, \tag{46}$$

where

$$\mathbf{q}_A = \begin{Bmatrix} u_A \\ v_A \\ w_A \\ \theta_{x,A} \\ \theta_{y,A} \end{Bmatrix} \tag{47}$$

is the generalized mechanical degree-of-freedom vector at the A -th control point, and ψ_A is the electric potential degree of freedom.

Using the isogeometric approximation in equation (46), the strain field can be written as

$$\boldsymbol{\varepsilon} = \mathbf{B}_u \mathbf{q}, \tag{48}$$

where \mathbf{q} is the global mechanical degree-of-freedom vector and \mathbf{B}_u is the strain–displacement matrix constructed from NURBS basis function derivatives. The membrane–bending and transverse shear components are

$$\boldsymbol{\varepsilon}_m = \mathbf{B}_m \mathbf{q}, \quad \boldsymbol{\gamma}_t = \mathbf{B}_t \mathbf{q}. \tag{49}$$

The electric field vector is approximated as

$$\mathbf{E} = \mathbf{B}_\varphi \boldsymbol{\psi}, \tag{50}$$

where $\boldsymbol{\psi}$ is the global electric potential vector and \mathbf{B}_φ contains the spatial derivatives of the NURBS basis functions.

Substitution of the isogeometric approximations into the weak form yields

$$\mathbf{K}_{uu} \mathbf{q} - \mathbf{K}_{u\varphi} \boldsymbol{\psi} - \omega^2 \mathbf{M} \mathbf{q} = \mathbf{0}, \quad \mathbf{K}_{\varphi u} \mathbf{q} + \mathbf{K}_{\varphi\varphi} \boldsymbol{\psi} = \mathbf{0}. \tag{51}$$

In equation (51), \mathbf{K}_{uu} is the mechanical stiffness matrix, $\mathbf{K}_{u\varphi}$ and $\mathbf{K}_{\varphi u}$ are the electromechanical coupling matrices, $\mathbf{K}_{\varphi\varphi}$ is the dielectric stiffness matrix, and \mathbf{M} is the mass matrix.

Eliminating the electric potential degrees of freedom from equation (51) gives the condensed eigenvalue problem

$$(\mathbf{K}_{eff} - \omega^2 \mathbf{M}) \mathbf{q} = \mathbf{0}, \quad (52)$$

where the effective stiffness matrix is

$$\mathbf{K}_{eff} = \mathbf{K}_{uu} - \mathbf{K}_{u\varphi} \mathbf{K}_{\varphi\varphi}^{-1} \mathbf{K}_{\varphi u}. \quad (53)$$

The global mass matrix is computed as

$$\mathbf{M} = \int_{\Omega} \mathbf{N}^T \mathbf{m}(z) \mathbf{N} d\Omega, \quad (54)$$

where \mathbf{N} collects the NURBS shape functions and $\mathbf{m}(z)$ is the inertia matrix obtained from the thickness integration of $\rho(z)$.

2.7. Numerical implementation: isogeometric formulation and fractional operator discretization

The proposed formulation simultaneously incorporates spatial fractional nonlocality, strain-gradient stiffening, electromechanical coupling, temporal fractional memory, and substrate interaction. The spatial nonlocality is introduced through the Riesz operator in equation (27), the strain-gradient contribution is introduced through equation (29), and the temporal memory effect is introduced through the Caputo operator in equation (33). Consequently, the final semi-discrete system contains classical stiffness, fractional nonlocal stiffness, strain-gradient stiffness, electromechanical coupling, dielectric stiffness, mass, and fractional-memory matrices.

2.7.1. Isogeometric field approximation

Let (ξ, η) denote the parametric coordinates of the isogeometric domain. The geometry mapping, displacement field, and electric potential are approximated using NURBS basis functions $\{R_A(\xi, \eta)\}_{A=1}^{n_{cp}}$ as

$$\mathbf{x}(\xi, \eta) = \sum_{A=1}^{n_{cp}} R_A(\xi, \eta) \mathbf{x}_A, \quad \mathbf{u}^h(\xi, \eta) = \sum_{A=1}^{n_{cp}} R_A(\xi, \eta) \mathbf{d}_A, \quad \phi^h(\xi, \eta) = \sum_{A=1}^{n_{cp}} R_A(\xi, \eta) \phi_A. \quad (55)$$

Here, n_{cp} is the number of control points, \mathbf{x}_A is the coordinate vector of the A -th control point, $\mathbf{d}_A = \{u_A, v_A, w_A, \theta_{x,A}, \theta_{y,A}\}^T$ is the mechanical degree-of-freedom vector, and ϕ_A is the electric potential degree of freedom. The Jacobian matrix of the mapping is

$$\mathbf{J} = \frac{\partial(x, y)}{\partial(\xi, \eta)}. \quad (56)$$

2.7.2. Generalized strain–displacement and electric-field matrices

Using the higher-order shear deformation kinematics defined in equations (8)–(13), the generalized strain vector is written as

$$\boldsymbol{\varepsilon}_g = \begin{Bmatrix} \boldsymbol{\varepsilon}_m \\ \boldsymbol{\gamma}_t \end{Bmatrix} = \mathbf{B}_g \mathbf{d}, \quad (57)$$

where \mathbf{d} is the global vector of mechanical degrees of freedom and \mathbf{B}_g is assembled from the NURBS basis function derivatives $R_{A,x}$, $R_{A,y}$, $R_{A,xx}$, $R_{A,yy}$, and $R_{A,xy}$.

The discretized electric field is obtained from $\mathbf{E} = -\nabla\Phi$ and written as

$$\mathbf{E}_g = \mathbf{B}_\phi \boldsymbol{\phi}, \quad \boldsymbol{\phi} = \{\phi_A\}, \quad (58)$$

where \mathbf{B}_ϕ contains the spatial derivatives of the NURBS basis functions and the through-thickness electric potential function defined in equation (15).

2.7.3. Discrete Laplacian and fractional matrix power

The discrete Laplacian matrix is constructed as

$$\mathbf{L} = \int_{\Omega} (\nabla \mathbf{N})^T (\nabla \mathbf{N}) d\Omega, \quad (59)$$

where \mathbf{N} collects the NURBS basis functions. The fractional matrix power required by the nonlocal operator is evaluated spectrally as

$$\mathbf{L} = \mathbf{Q} \boldsymbol{\Lambda} \mathbf{Q}^{-1}, \quad \mathbf{L}^{\alpha/2} = \mathbf{Q} \boldsymbol{\Lambda}^{\alpha/2} \mathbf{Q}^{-1}. \quad (60)$$

To avoid numerical difficulty associated with zero or near-zero eigenvalues, a small regularization parameter ε is introduced as

$$\boldsymbol{\Lambda} \leftarrow \boldsymbol{\Lambda} + \varepsilon \mathbf{I}, \quad \varepsilon > 0. \quad (61)$$

Algorithm: fractional nonlocal strain–gradient IGA with temporal memory

Input: (a, b, h) , porosity type, material data, (k_w, k_s) , (α, β) , (ℓ_f, ℓ_g) , and regularization parameter ε .

- (i) Build NURBS geometry, control net, knot vectors, and basis functions.
- (ii) Evaluate basis derivatives and construct \mathbf{B}_g and \mathbf{B}_ϕ .
- (iii) Assemble \mathbf{M}_{uu} , \mathbf{K}_{cl} , $\mathbf{K}_{u\phi}$, $\mathbf{K}_{\phi\phi}$, and $\mathbf{C}_{uu}^{(\beta)}$.
- (iv) Assemble \mathbf{L} and compute $\mathbf{L}^{\alpha/2}$.
- (v) Assemble $\mathbf{K}_{nl}^{(\alpha)}$ and \mathbf{K}_{sg} .
- (vi) Form \mathbf{K}_{uu} and compute $\mathbf{K}_{eff} = \mathbf{K}_{uu} - \mathbf{K}_{u\phi}\mathbf{K}_{\phi\phi}^{-1}\mathbf{K}_{\phi u}$.
- (vii) Apply boundary conditions and solve the eigenvalue or fractional dynamic problem.
- (viii) Output natural frequencies, mode shapes, and parametric trends.

Figure 2: Combined computational workflow for the proposed fractional nonlocal strain–gradient isogeometric formulation.

2.7.4. Global matrix system

After spatial discretization and thickness integration, the coupled semi-discrete electromechanical system is obtained as

$$\mathbf{M}_{uu}\ddot{\mathbf{d}} + \mathbf{C}_{uu}^{(\beta)} {}^C D_t^\beta \mathbf{d} + \mathbf{K}_{uu}\mathbf{d} - \mathbf{K}_{u\phi}\boldsymbol{\phi} = \mathbf{0}, \quad \mathbf{K}_{\phi u}\mathbf{d} + \mathbf{K}_{\phi\phi}\boldsymbol{\phi} = \mathbf{0}. \quad (62)$$

The mechanical stiffness matrix is decomposed as

$$\mathbf{K}_{uu} = \mathbf{K}_{cl} + \mathbf{K}_{nl}^{(\alpha)} + \mathbf{K}_{sg} + \mathbf{K}_f, \quad (63)$$

where \mathbf{K}_{cl} is the classical stiffness matrix, $\mathbf{K}_{nl}^{(\alpha)}$ is the fractional nonlocal stiffness matrix, \mathbf{K}_{sg} is the strain-gradient stiffness matrix, and \mathbf{K}_f is the foundation stiffness matrix.

The classical stiffness matrix, fractional nonlocal stiffness matrix, strain-gradient stiffness matrix, and fractional memory matrix are respectively defined as

$$\begin{aligned} \mathbf{K}_{cl} &= \int_{\Omega} \mathbf{B}_g^T \mathbf{C}_r(z) \mathbf{B}_g \, d\Omega, & \mathbf{K}_{nl}^{(\alpha)} &= \ell_f^\alpha \int_{\Omega} \mathbf{B}_g^T \mathbf{C}_r(z) \mathbf{L}^{\alpha/2} \mathbf{B}_g \, d\Omega, \\ \mathbf{K}_{sg} &= \ell_g^2 \int_{\Omega} (\nabla \mathbf{B}_g)^T \mathbf{C}_r(z) (\nabla \mathbf{B}_g) \, d\Omega, & \mathbf{C}_{uu}^{(\beta)} &= \int_{\Omega} \mathbf{B}_g^T \mathbf{C}_v(z) \mathbf{B}_g \, d\Omega. \end{aligned} \quad (64)$$

The fractional-memory contribution in equation (64) enters the dynamic equilibrium equation through the Caputo fractional derivative term in equation (62).

The electromechanical coupling and dielectric matrices are

$$\mathbf{K}_{u\phi} = \int_{\Omega} \mathbf{B}_g^T \mathbf{e}_r(z) \mathbf{B}_\phi \, d\Omega, \quad \mathbf{K}_{\phi\phi} = \int_{\Omega} \mathbf{B}_\phi^T \mathbf{k}_r(z) \mathbf{B}_\phi \, d\Omega. \quad (65)$$

The consistent mass matrix is

$$\mathbf{M}_{uu} = \int_{\Omega} \left(\int_{-h/2}^{h/2} \rho(z) \, dz \right) \mathbf{N}^T \mathbf{N} \, d\Omega. \quad (66)$$

2.7.5. Electric-potential condensation

From equation (62), the electric potential vector is obtained as

$$\boldsymbol{\phi} = -\mathbf{K}_{\phi\phi}^{-1} \mathbf{K}_{\phi u} \mathbf{d}. \quad (67)$$

Substituting equation (67) into equation (62) gives the condensed fractional-in-time mechanical system

$$\mathbf{M}_{uu}\ddot{\mathbf{d}} + \mathbf{C}_{uu}^{(\beta)} {}^C D_t^\beta \mathbf{d} + \mathbf{K}_{eff}\mathbf{d} = \mathbf{0}, \quad (68)$$

where

$$\mathbf{K}_{eff} = \mathbf{K}_{uu} - \mathbf{K}_{u\phi} \mathbf{K}_{\phi\phi}^{-1} \mathbf{K}_{\phi u}. \quad (69)$$

When $\mathbf{C}_{uu}^{(\beta)} = \mathbf{0}$, equation (68) reduces to the standard eigenvalue problem

$$\mathbf{K}_{eff} \mathbf{d} = \omega^2 \mathbf{M}_{uu} \mathbf{d}. \quad (70)$$

For $\mathbf{C}_{uu}^{(\beta)} \neq \mathbf{0}$, the free response is governed by a fractional-order dynamic system, and frequency indicators may be extracted by harmonic approximation or time integration followed by spectral identification.

2.8. Algorithmic implementation and computational workflow

The computational workflow for implementing the fractional nonlocal strain–gradient isogeometric formulation with temporal memory is summarized as follows:

- (i) Specify the geometry (a, b, h) , porosity distribution type, material properties, foundation parameters (k_w, k_s) , spatial fractional order α , temporal memory order β , and length-scale parameters (ℓ_f, ℓ_g) .
- (ii) Construct the NURBS knot vectors, control points, basis functions, and weights in the ξ - and η -directions.
- (iii) Evaluate the NURBS basis functions and their derivatives required for the HSDT strain–displacement matrix \mathbf{B}_g and the electric-field matrix \mathbf{B}_ϕ .
- (iv) Assemble the classical stiffness matrix, fractional nonlocal stiffness matrix, strain-gradient stiffness matrix, and fractional-memory matrix using equation (64).
- (v) Assemble the electromechanical coupling matrix, dielectric matrix, and consistent mass matrix using equation (65) and equation (66).
- (vi) Construct the discrete Laplacian matrix using equation (59) and evaluate its fractional power using equation (60).
- (vii) Form the global mechanical stiffness matrix using equation (63).
- (viii) Condense the electric potential degrees of freedom using equation (67) to obtain the effective stiffness matrix in equation (69).
- (ix) Impose the essential boundary constraints at the control-point level.
- (x) Solve the standard eigenvalue problem in equation (70) when the temporal fractional memory term is neglected, or solve the fractional dynamic system in equation (68) when memory effects are included.
- (xi) Post-process the natural frequencies, mode shapes, percentage-error validation results, and parametric responses.

Figure 2 summarizes the full numerical procedure. The two separate workflow figures in the previous version have been combined into one figure to improve compactness and avoid unnecessary figure duplication.

2.8.1. Computational cost and conditioning

Let N denote the total number of control points and p the polynomial degree of the NURBS basis. The main computational requirements are summarized as follows:

- (i) Matrix assembly typically scales with $O(Np^2)$, depending on quadrature and basis continuity.
- (ii) Dense eigen-decomposition of the discrete Laplacian matrix \mathbf{L} scales as $O(N^3)$.
- (iii) For parametric sweeps, the fractional matrix power $\mathbf{L}^{\alpha/2}$ may be computed once for a fixed mesh and reused.
- (iv) The dominant cost in large simulations arises from sparse solution of the eigenvalue problem or from fractional time integration.

The discrete Laplacian matrix \mathbf{L} is symmetric positive semi-definite. The fractional matrix power may amplify conditioning according to

$$\kappa(\mathbf{L}^{\alpha/2}) = \frac{\lambda_{\max}^{\alpha/2}}{\lambda_{\min}^{\alpha/2}}. \quad (71)$$

To avoid numerical singularity caused by vanishing eigenvalues, the regularization

$$\lambda_i^{\alpha/2} \rightarrow (\lambda_i + \varepsilon)^{\alpha/2} \quad (72)$$

is adopted. This regularization preserves positivity and improves numerical conditioning.

Table 2: Elastic coefficients of PZT constituents used for validation.

Coefficient	PZT-4	PZT-5H
	<i>Elastic coefficients (GPa)</i>	
$c_{11} = c_{22}$	138.499	99.201
c_{12}	77.371	54.016
c_{13}	73.643	50.778
c_{33}	114.745	86.856
c_{55}	25.600	21.100
c_{66}	30.600	22.600

Table 3: Piezoelectric, dielectric, and density properties of PZT constituents.

Property	PZT-4	PZT-5H
	<i>Piezoelectric coefficients (C m⁻²)</i>	
e_{31}	-5.200	-7.209
e_{33}	15.080	15.118
e_{15}	12.720	12.322
	<i>Dielectric coefficients</i>	
k_{11}	1.306	1.530
k_{33}	1.115	1.500
	<i>Density (kg m⁻³)</i>	
ρ	7600	7750

Note: Elastic coefficients are in GPa, piezoelectric coefficients are in C m⁻², and dielectric coefficients are scaled by 10⁻⁹ C²m⁻²N⁻¹.

2.8.2. Stability and parameter range

Provided that $\ell_f^\alpha > 0$, $\ell_g^2 > 0$, and $C_r(z)$ is positive definite, the effective stiffness matrix remains coercive after essential boundary constraints are imposed. The fractional memory matrix $C_{uu}^{(\beta)}$ contributes hereditary dissipation and improves the stability of time-domain simulations.

In the parametric studies, the spatial fractional order is varied within $0.6 \leq \alpha \leq 1.0$, the temporal memory order is selected within $0 < \beta \leq 1$, and the strain-gradient ratio is examined within $0 \leq \ell_g/h \leq 0.3$.

3. Numerical results and discussion

The free vibration characteristics of porous functionally graded piezoelectric microplates resting on elastic substrates are investigated using the proposed fractional nonlocal strain–gradient isogeometric formulation. Unless otherwise stated, the reference parameters are $a/h = 20$, $\alpha = 0.9$, $\ell_g/h = 0.1$, and simply supported boundary conditions on all edges.

3.1. Dimensionless parameters and boundary conditions

To facilitate comparison with existing studies, the dimensionless frequency and foundation coefficients are defined as

$$\bar{\omega} = \omega \frac{a^2}{h} \sqrt{\frac{\rho_{\text{ref}}}{E_{\text{ref}}}}, \quad K_w = \frac{a^4 k_w}{E_{\text{ref}} h^3}, \quad K_s = \frac{a^2 k_s}{E_{\text{ref}} h^3}, \quad (73)$$

where E_{ref} and ρ_{ref} denote the reference Young’s modulus and density of the base piezoelectric material, respectively. The parameters k_w and k_s are the Winkler and Pasternak foundation parameters.

For a simply supported microplate, the boundary conditions are imposed as

$$\text{SSSS:} \quad (v, w, \theta_y)|_{x=0,a} = 0, \quad (u, w, \theta_x)|_{y=0,b} = 0. \quad (74)$$

3.2. Material properties used for validation

Tables 2 and 3 list the PZT-4 and PZT-5H material properties used in the benchmark validation. These properties are adopted to compare the present nondimensional frequencies with the reference solutions of Phong and Hung [17].

Table 2 provides the elastic stiffness coefficients used in the validation cases, while Table 3 summarizes the piezoelectric coefficients, dielectric coefficients, and density values. These material data are used in computing the nondimensional frequency parameter defined in equation (73).

3.3. Model validation and convergence analysis

The numerical accuracy and robustness of the formulation are verified through classical-limit comparison, mesh convergence assessment, and strain-gradient benchmark validation.

Table 4: Classical-limit validation of the functionally graded piezoelectric square microplate under SSSS boundary conditions ($a/h = 100, \ell_f = \ell_g = 0, K_w = K_s = 0$).

α	V_0 (V)	p	Present	Ref. [17]	Error (%)
0	-500	0.2	6.12786	6.20648	1.267
0	-500	1.0	5.40481	6.00370	9.975
0	-500	5.0	4.98992	5.85518	14.778
0	0	0.2	6.08694	6.03123	0.924
0	0	1.0	5.35868	5.81866	7.906
0	0	5.0	4.94024	5.66198	12.748
0.2	500	0.2	5.76802	5.89806	2.205
0.2	500	1.0	4.99018	5.61511	11.130
0.2	500	5.0	4.54375	5.40780	15.978

Table 5: Mesh convergence of selected classical-limit frequency results.

Case	9×9	11×11	13×13
$\alpha = 0, V_0 = -500 \text{ V}, p = 0.2$	6.17082	6.14374	6.12786
$\alpha = 0, V_0 = 0 \text{ V}, p = 0.2$	6.13018	6.10292	6.08694
$\alpha = 0.2, V_0 = 500 \text{ V}, p = 0.2$	5.81282	5.78473	5.76802

3.3.1. Validation in the classical limit

The classical local limit is recovered by setting $\ell_f = 0, \ell_g = 0$, and $\mathbf{C}_{uu}^{(\beta)} = \mathbf{0}$ in equation (68). Under these conditions, the formulation reduces to the classical electromechanical plate model. The computed dimensionless frequency parameter in equation (73) is compared with the refined plate theory results reported by Phong and Hung [17].

The percentage error is computed as

$$\text{Error}(\%) = \left| \frac{\bar{\omega}_{\text{Present}} - \bar{\omega}_{\text{Ref}}}{\bar{\omega}_{\text{Ref}}} \right| \times 100. \tag{75}$$

Table 4 presents selected classical-limit comparisons using the refined 13×13 mesh.

The comparison in Table 4 shows that the present results are closer to the reference values for lower gradation indices, while larger deviations occur for higher gradation indices. These differences may be associated with differences in gradation assumptions, electric boundary treatment, or numerical implementation details. Therefore, the classical-limit comparison is treated as a consistency assessment, while the strain-gradient benchmark in Table 6 provides the stronger validation evidence for the present implementation.

3.3.2. Mesh convergence study

To assess numerical convergence, the first nondimensional frequency is computed using $9 \times 9, 11 \times 11$, and 13×13 IGA control-point discretizations. The results are summarized in Table 5.

Table 5 indicates that the frequency values approach a stable value as the mesh is refined. Hence, the 13×13 mesh is adopted in the final computations.

3.3.3. Validation of strain-gradient implementation

Further validation is performed using the metal foam microplate benchmark reported by Phong and Hung [17]. The material parameters are

$$E_1 = 200 \text{ GPa}, \quad \nu_1 = 0.33, \quad \rho_1 = 7850 \text{ kg/m}^3. \tag{76}$$

The normalized frequency parameter is defined as

$$\hat{\omega} = \omega h \sqrt{\frac{\rho_1}{E_1}}. \tag{77}$$

As shown in Table 6, the maximum percentage error is approximately 0.332%. This close agreement verifies the implementation of the strain-gradient stiffness contribution and confirms the reliability of the present isogeometric formulation for size-dependent vibration analysis.

3.3.4. Summary of validation

The validation studies demonstrate that:

- (i) the formulation correctly reduces to the classical local model when the size-dependent parameters are suppressed;

Table 6: Percentage-error validation of the first normalized frequency of the metal foam microplate benchmark ($e_0 = 0.2, a/h = 10$).

BCs	Porosity distribution	ℓ/h	Present	Ref. [17]	Error (%)
SSSS	Uniform	0.0	0.0562	0.0562	0.000
SSSS	Uniform	0.1	0.0601	0.0602	0.166
SSSS	Uniform	0.2	0.0704	0.0706	0.283
SSSS	Uniform	0.5	0.1202	0.1206	0.332
SSSS	Uniform	1.0	0.2202	0.2206	0.181
SSSS	Symmetric	0.0	0.0579	0.0579	0.000
SSSS	Symmetric	0.1	0.0616	0.0618	0.324
SSSS	Symmetric	0.2	0.0722	0.0721	0.139
SSSS	Symmetric	0.5	0.1216	0.1220	0.328
SSSS	Symmetric	1.0	0.2215	0.2212	0.136
SSSS	Asymmetric	0.0	0.0565	0.0565	0.000
SSSS	Asymmetric	0.1	0.0604	0.0604	0.000
SSSS	Asymmetric	0.2	0.0707	0.0709	0.282
SSSS	Asymmetric	0.5	0.1205	0.1209	0.331
SSSS	Asymmetric	1.0	0.2207	0.2211	0.181

Table 7: Computed dimensionless natural frequencies for D-I porosity distribution.

η	Mode 1	Mode 2	Mode 3	Mode 4	Mode 5	Mode 6
0.10	4.176178	10.572674	10.572674	14.543362	14.543362	16.192124
0.20	4.158111	10.516870	10.516870	14.292429	14.292429	16.088999
0.30	4.141595	10.461535	10.461535	14.030459	14.030459	15.982542
0.40	4.127153	10.406490	10.406490	13.756769	13.756769	15.870896
0.50	4.115486	10.351084	10.351084	13.470897	13.470897	15.750558
0.55	4.110977	10.322772	10.322772	13.323388	13.323388	15.685191

(ii) the computed frequencies converge with mesh refinement;

(iii) the strain-gradient implementation agrees closely with the benchmark solution of Phong and Hung [17].

These results provide a reliable computational basis for the subsequent parametric studies.

3.4. Effect of porosity coefficient and porosity distribution

Tables 7 and 8 present the first six dimensionless natural frequencies for the D-I, D-II, and D-III porosity distributions under different values of the porosity coefficient.

Table 7 presents the computed dimensionless natural frequencies for the D-I porosity distribution, while Table 8 presents the corresponding results for the D-II and D-III porosity distributions. The results show that increasing the porosity coefficient reduces the natural frequencies because porosity weakens the effective stiffness of the microplate. The D-I distribution generally gives the highest frequencies, while the D-II distribution gives the lowest frequencies, indicating that the through-thickness location of porosity strongly influences the stiffness and vibration response.

3.5. Influence of spatial fractional order, temporal memory order, and strain-gradient parameter

Table 9 summarizes the effects of the spatial fractional order α , temporal memory order β , and strain-gradient ratio ℓ_g/h on the first dimensionless natural frequency.

The first block of Table 9 shows that increasing α increases the natural frequency. This indicates that the response moves from a stronger nonlocal regime toward a weaker nonlocal regime, thereby reducing the softening effect associated with long-range interactions. The second block shows that the memory order β produces a mild frequency shift because the temporal memory term mainly affects the dynamic response through hereditary dissipation. The third block shows that increasing ℓ_g/h significantly increases the frequency because strain-gradient elasticity introduces additional microstructural stiffness.

Table 8: Computed dimensionless natural frequencies for D-II and D-III porosity distributions.

Pattern	η	Mode 1	Mode 2	Mode 3	Mode 4	Mode 5	Mode 6
D-II	0.10	4.039808	10.245095	10.245095	14.546778	14.546778	15.728351
D-II	0.20	3.869178	9.819627	9.819627	14.305111	14.305111	15.098706
D-II	0.30	3.680067	9.342246	9.342246	14.061835	14.061835	14.387492
D-II	0.40	3.467695	8.798375	8.798375	13.571162	13.823007	13.823007
D-II	0.50	3.225280	8.166537	8.166537	12.614731	13.602657	13.602657
D-II	0.55	3.089977	7.808106	7.808106	12.068267	13.509424	13.509424
D-III	0.10	4.127087	10.455963	10.455963	14.542926	14.542926	16.028129
D-III	0.20	4.055140	10.273814	10.273814	14.289014	14.289014	15.749284
D-III	0.30	3.979208	10.081582	10.081582	14.021012	14.021012	15.455023
D-III	0.40	3.898661	9.877677	9.877677	13.736697	13.736697	15.142923
D-III	0.50	3.812788	9.660299	9.660299	13.433543	13.433543	14.810233
D-III	0.55	3.767618	9.545961	9.545961	13.274063	13.274063	14.635257

Table 9: Combined influence of spatial fractional order α , temporal memory order β , and strain-gradient parameter ℓ_g/h on the first dimensionless frequency.

Spatial fractional effect		Temporal memory effect		Strain-gradient effect	
α	$\bar{\omega}$	β	$\bar{\omega}$	ℓ_g/h	$\bar{\omega}$
0.6	5.412	0.6	5.732	0.00	5.864
0.7	5.568	0.7	5.784	0.05	5.942
0.8	5.721	0.8	5.828	0.10	6.082
0.9	5.864	0.9	5.864	0.20	6.348
1.0	5.990	1.0	5.900	0.30	6.721

Table 10: Effect of elastic foundation parameters on nondimensional natural frequency ($e_0 = 0.2$, D-I distribution).

k_w	k_s	$\bar{\omega}$
0	0	14.612
50	5	15.104
100	10	15.498
200	20	15.892
300	30	16.113

Table 11: Effect of nondimensional elastic foundation parameters on nondimensional natural frequency ($e_0 = 0.2$, D-I distribution, SSSS, $a/h = 10$, $\ell_g/h = 0.1$).

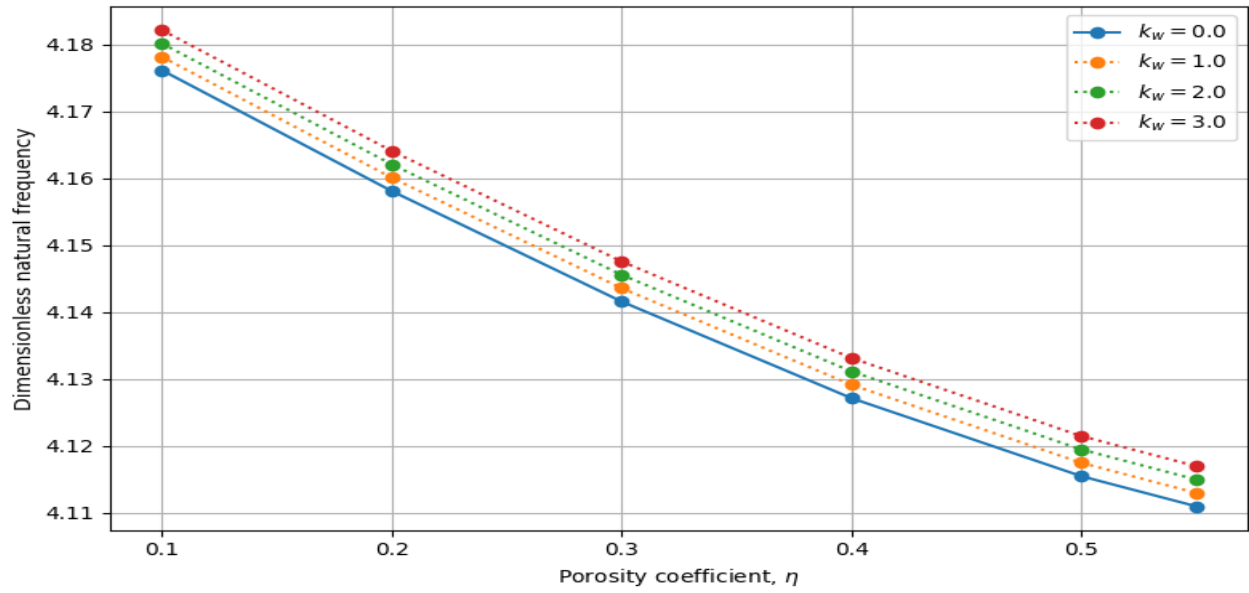
$K_w \backslash K_s$	0	0.05	0.1	0.2
0	0.0429	0.0429	0.0429	0.0429
1	0.0429	0.0429	0.0429	0.0429
2	0.0429	0.0429	0.0429	0.0429
3	0.0429	0.0429	0.0429	0.0430

3.6. Effect of elastic foundation

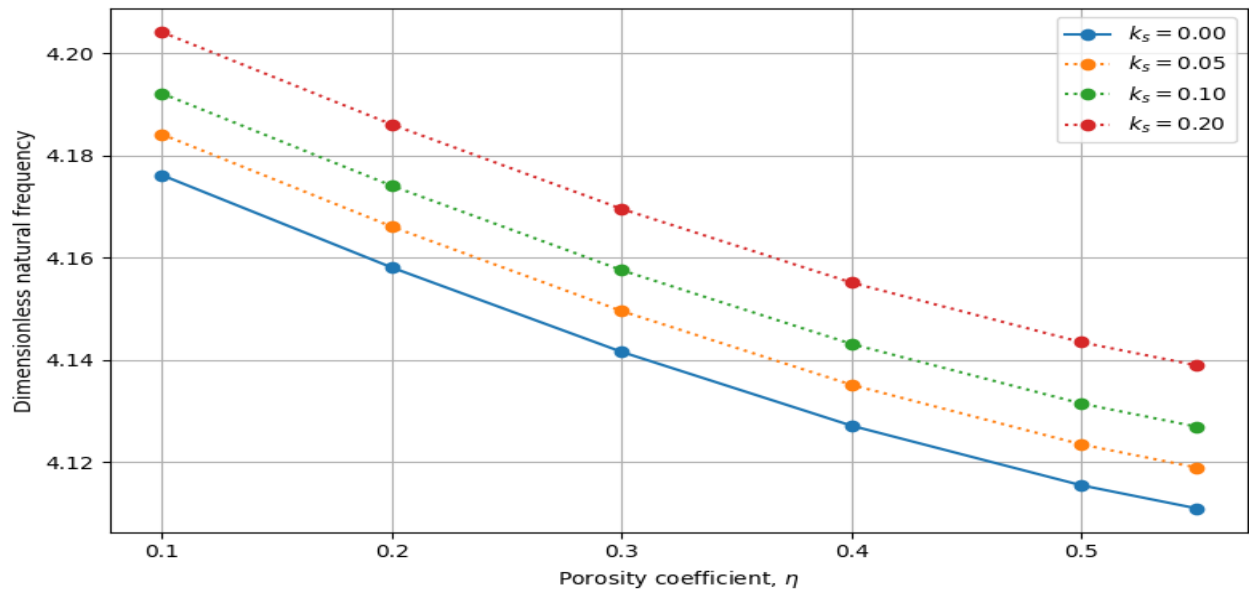
The influence of the Winkler stiffness k_w and Pasternak shear parameter k_s is examined in Tables 10 and 11. The corresponding graphical trends are shown in Figure 3.

Table 10 shows that the natural frequency increases as the dimensional foundation parameters increase. This confirms that the elastic substrate enhances the effective stiffness of the plate–foundation system. Table 11 further indicates that, within the selected nondimensional range, the foundation contribution is relatively weak compared with the intrinsic stiffness of the microplate. Nevertheless, the general trend still shows a slight frequency increase as K_w and K_s increase.

Figure 3(a) shows that increasing the Winkler stiffness causes a moderate increase in frequency. Figure 3(b) shows that the



(a)



(b)

Figure 3: Influence of elastic foundation parameters on the dimensionless natural frequency of the porous FG piezoelectric microplate: (a) Winkler foundation stiffness effect and (b) Pasternak shear parameter effect.

Table 12: Effect of applied electric voltage on nondimensional natural frequency ($e_0 = 0.2$, D-I distribution).

V_0 (V)	α	k_w	$\bar{\omega}$
0	0.9	100	15.498
25	0.9	100	15.612
50	0.9	100	15.781
75	0.9	100	15.904
100	0.9	100	16.021

Pasternak shear parameter produces a more visible frequency increase because it introduces shear interaction within the supporting medium.

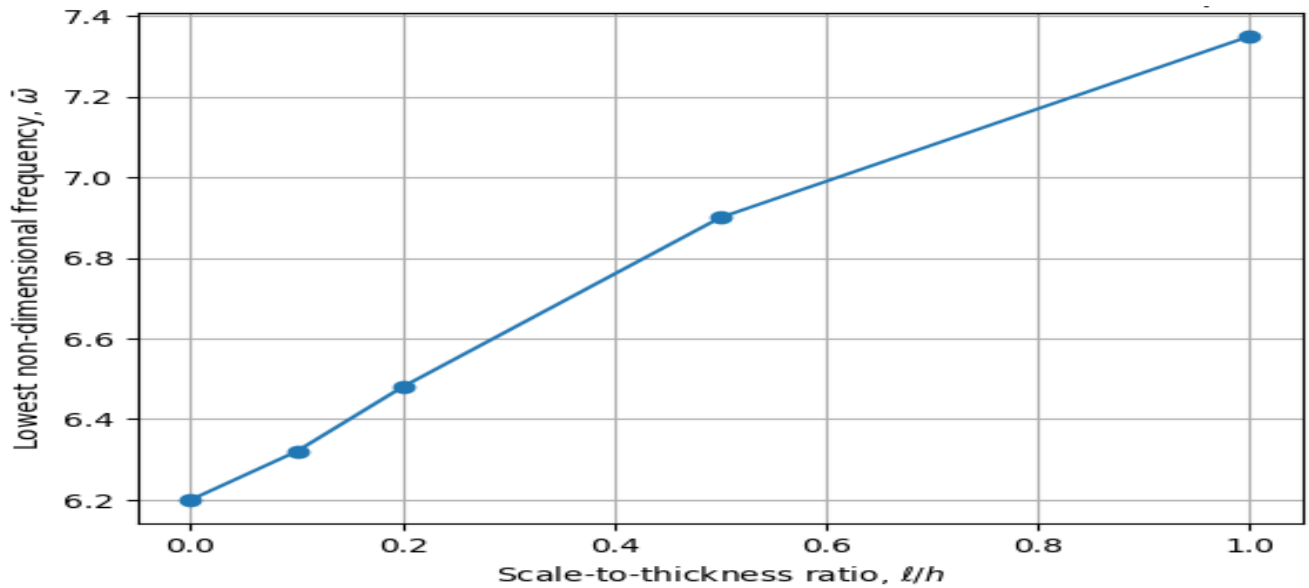


Figure 4: Influence of the scale-to-thickness ratio (l/h) on the lowest nondimensional vibration frequency of FG piezoelectric microplates with different boundary conditions.

Table 13: Combined parametric effect of porosity, fractional order, and foundation stiffness.

e_0	α	k_w	$\bar{\omega}$
0.10	0.7	100	15.212
0.10	0.9	100	15.498
0.30	0.7	100	14.812
0.30	0.9	100	15.103
0.30	0.9	200	15.481

3.7. Effect of applied electric voltage

The applied voltage influences the vibration response through the electromechanical coupling terms in equation (19) and through the effective stiffness matrix in equation (69). The voltage effect is summarized in Table 12, while the combined influence of porosity, fractional order, and foundation stiffness is summarized in Table 13.

Table 12 shows that increasing the applied voltage increases the nondimensional frequency for the selected parameter range. This indicates that the applied electric field contributes additional electromechanical stiffness to the porous piezoelectric microplate.

Table 13 shows the combined influence of porosity, fractional order, and foundation stiffness. Increasing the porosity coefficient reduces the frequency, while increasing the fractional order and foundation stiffness increases the frequency. This confirms that the vibration response is governed by the combined effects of porosity-induced stiffness reduction, nonlocal interaction, and substrate-induced stiffness enhancement.

Figure 4 shows that the nondimensional frequency increases with the scale-to-thickness ratio. This trend confirms the stiffening role of the strain-gradient length-scale parameter.

3.8. General discussion

The numerical results show that the vibration behaviour of the porous functionally graded piezoelectric microplate is governed by competing stiffness-reducing and stiffness-enhancing mechanisms. Increasing porosity reduces the effective stiffness and lowers the natural frequencies. In contrast, increasing the strain-gradient parameter, elastic foundation stiffness, and applied electric voltage increases the effective stiffness and raises the frequency values.

The spatial fractional order regulates the intensity of long-range interaction, while the temporal fractional order controls the hereditary memory effect associated with fractional viscoelasticity. The results also show that size-dependent effects are important in microscale vibration analysis and should not be neglected in the design of porous piezoelectric microplates for MEMS, sensors, actuators, and energy-harvesting devices.

4. Conclusion

This study developed a fractional nonlocal strain–gradient isogeometric formulation for the free vibration analysis of porous functionally graded piezoelectric microplates resting on elastic substrates. The formulation combined higher-order shear deformation theory, fractional spatial nonlocality, strain-gradient elasticity, temporal fractional viscoelastic memory, piezoelectric coupling, and Winkler-Pasternak foundation interaction within a unified electromechanical framework. The governing equations were derived from Hamilton’s variational principle and discretized using isogeometric analysis to satisfy the higher-order continuity requirements associated with the fractional and gradient operators.

The formulation was validated by reducing the model to classical and strain-gradient benchmark cases and comparing the computed nondimensional frequencies with published reference results. The inclusion of percentage-error analysis confirmed the accuracy of the strain-gradient implementation, with the metal foam microplate benchmark showing a maximum percentage deviation of approximately 0.332%. The mesh convergence results also confirmed that the adopted isogeometric discretization provides stable and reliable frequency predictions.

The parametric results showed that increasing the porosity coefficient reduces the natural frequencies because porosity weakens the effective stiffness of the microplate. In contrast, increasing the strain-gradient length-scale parameter and elastic foundation stiffness increases the natural frequencies due to additional microstructural and substrate-induced stiffness. The spatial fractional order was found to regulate the strength of long-range nonlocal interaction, while the temporal memory order modified the vibration response through hereditary viscoelastic effects. The applied electric voltage also influenced the effective stiffness through electromechanical coupling.

The findings indicate that the vibration characteristics of porous piezoelectric microplates can be tuned through porosity design, length-scale parameters, elastic foundation stiffness, and electric voltage control. Therefore, the proposed formulation provides a useful computational framework for the analysis and design of MEMS devices, smart sensors, micro-actuators, resonators, and micro-energy harvesting systems where size-dependent, electromechanical, and substrate effects are significant.

Data availability

All data used in this work are simulated and were generated during the numerical implementation of the proposed formulation. The simulated datasets and computational results supporting the findings of this study are available from the corresponding author upon reasonable request.

Declaration of competing interest

The authors declare that no competing financial, professional, or personal interests are associated with the publication of this manuscript.

Funding statement

This research received no external funding.

References

- [1] F. Yang, A. C. M. Chong, D. C. C. Lam & P. Tong, “Couple stress based strain gradient theory for elasticity”, *International Journal of Solids and Structures* **39** (2002) 2731. [https://doi.org/10.1016/S0020-7683\(02\)00152-X](https://doi.org/10.1016/S0020-7683(02)00152-X).
- [2] D. C. C. Lam, F. Yang, A. C. M. Chong, J. Wang & P. Tong, “Experiments and theory in strain gradient elasticity”, *Journal of the Mechanics and Physics of Solids* **51** (2003) 1477. [https://doi.org/10.1016/S0022-5096\(03\)00053-X](https://doi.org/10.1016/S0022-5096(03)00053-X).
- [3] A. C. Eringen, “On differential equations of nonlocal elasticity and solutions of screw dislocation and surface waves”, *Journal of Applied Physics* **54** (1983) 4703. <https://doi.org/10.1063/1.332803>.
- [4] A. C. Eringen, *Nonlocal continuum field theories*, Springer, New York, USA, 2002. <https://doi.org/10.1007/b97697>.
- [5] C.-P. Wu & E.-L. Lin, “Free vibration analysis of porous functionally graded piezoelectric microplates resting on an elastic medium subjected to electric voltages”, *Archives of Mechanics* **74** (2022) 463. <https://doi.org/10.24423/aom.4150>.
- [6] Y. Liang, S. Zheng & D. Chen, “Isogeometric analysis of graphene-reinforced functionally gradient piezoelectric plates resting on Winkler elastic foundations”, *Materials* **15** (2022) 5727. <https://doi.org/10.3390/ma15165727>.
- [7] T. J. R. Hughes, J. A. Cottrell & Y. Bazilevs, “Isogeometric analysis: CAD, finite elements, NURBS, exact geometry and mesh refinement”, *Computer Methods in Applied Mechanics and Engineering* **194** (2005) 4135. <https://doi.org/10.1016/j.cma.2004.10.008>.
- [8] S. Thai, H.-T. Thai, T. P. Vo & V. I. Patel, “Size-dependent behaviour of functionally graded microplates based on the modified strain gradient elasticity theory and isogeometric analysis”, *Computers & Structures* **190** (2017) 219. <https://doi.org/10.1016/j.compstruc.2017.05.014>.
- [9] C. H. Thai, A. J. M. Ferreira & P. Phung-Van, “Size dependent free vibration analysis of multilayer functionally graded GPLRC microplates based on modified strain gradient theory”, *Composites Part B: Engineering* **169** (2019) 174. <https://doi.org/10.1016/j.compositesb.2019.02.048>.
- [10] L. Lu, X. Guo & J. Zhao, “A unified size-dependent plate model based on nonlocal strain gradient theory including surface effects”, *Applied Mathematical Modelling* **68** (2019) 583. <https://doi.org/10.1016/j.apm.2018.11.023>.

- [11] M. Di Paola, F. Marino & M. Zingales, "A generalized model of elastic foundation based on long-range interactions: Integral and fractional formulation", *International Journal of Solids and Structures* **46** (2009) 3124. <https://doi.org/10.1016/j.ijsolstr.2009.03.024>.
- [12] Z. Rahimi, S. Shafiei, W. Sumelka & G. Rezazadeh, "Fractional strain energy and its application to the free vibration analysis of a plate", *Microsystem Technologies* **25** (2019) 2229. <https://doi.org/10.1007/s00542-018-4087-8>.
- [13] S. A. Jimoh, O. O. Niyi, A. S. Adeoye & E. C. Ajila, "Multiscale fractal-crack interaction in orthotropic plates on fractional foundations using extended finite element method and fox H-functions", *General Letters in Mathematics (GLM)* **15** (2025) 3. https://openurl.ebsco.com/EPDB%3Aagd%3A3%3A26695219/detailv2?sid=ebsco%3Aplink%3Ascholar&id=ebsco%3Aagd%3A191095750&crl=c&link_origin=scholar.google.com.
- [14] P. L. Pasternak, *On a New Method of Analysis of an Elastic Foundation by Means of Two Foundation Constants*, Gosudarstvennoe Izdatel'stvo Literaturi po Stroitel'stvu i Arkhitekture, Moscow, Russia, 1954. <https://www.semanticscholar.org/paper/On-a-new-method-of-analysis-of-an-elastic-by-means-Pasternak/5c0e1c492097b05b3aee9916eccce6296a5ef908>
- [15] A. D. Kerr, "Elastic and viscoelastic foundation models", *Journal of Applied Mechanics* **31** (1964) 491. <https://doi.org/10.1115/1.3629667>.
- [16] A. D. Kerr, "A study of a new foundation model", *Acta Mechanica* **1** (1965) 135. <https://doi.org/10.1007/BF01174308>.
- [17] L. T. Phong & P. T. Hung, "Size-dependent free vibration of porous piezoelectric microplate resting on an elastic substrate using MSGT, HSDT, and IGA", *Vietnam Journal of Mechanics* **47** (2025) 340. <https://doi.org/10.15625/0866-7136/23029>.